IRIS AperTO

UNIVERSITÀ DEGLI STUDI DI TORINO

AperTO - Archivio Istituzionale Open Access dell'Università di Torino

Post-eruption morphological evolution and vegetation dynamics of the Blanco River, southern Chile

This is the author's manuscript

Original Citation:

Availability:

This version is available http://hdl.handle.net/2318/1765584 since 2023-11-24T14:11:36Z

Published version:

DOI:10.1016/j.jsames.2020.102809

Terms of use:

Open Access

Anyone can freely access the full text of works made available as "Open Access". Works made available under a Creative Commons license can be used according to the terms and conditions of said license. Use of all other works requires consent of the right holder (author or publisher) if not exempted from copyright protection by the applicable law.

(Article begins on next page)

14 May 2024

IRIS AperTO

UNIVERSITÀ DEGLI STUDI DI TORINO

This is the author's final version of the contribution published as:

[Andrés Iroumé, Alberto Paredes, Matteo Garbarino, Donato Morresi, Ramon J. Batalla, Post-eruption morphological evolution and vegetation dynamics of the Blanco River, southern Chile, Journal of South American Earth Sciences, 104:2020,102809, doi:10.1016/j.jsames.2020.102809.]

The publisher's version is available at:

[https://www.sciencedirect.com/science/article/abs/pii/S0895981120303527]

When citing, please refer to the published version.

Link to this full text:

[http://hdl.handle.net/2318/1765584]

This full text was downloaded from iris-Aperto: https://iris.unito.it/

iris-AperTO

University of Turin's Institutional Research Information System and Open Access Institutional Repository

POST-ERUPTION MORPHOLOGICAL EVOLUTION AND VEGETATION DYNAMICS OF THE BLANCO RIVER, SOUTHERN CHILE

Andrés Iroumé[1*], Alberto Paredes[1,2], Matteo Garbarino[3], Donato Morresi[3], Ramon J. Batalla[1,4,5]

[1] Universidad Austral de Chile, Laboratorio de Hidromorfología, Facultad de Ciencias Forestales y Recursos Naturales, Valdivia (Chile)
[2] Graduate School, Facultad de Ciencias, Universidad Austral de Chile, Valdivia (Chile)
[3] Department of Agricultural, Forest and Food Sciences, University of Torino, Torino (Italy)
[4] Fluvial Dynamics Research Group –RIUS, University of Lleida, Catalonia (Spain)
[5] Catalan Institute for Water Research, Girona, Catalonia (Spain)

*Corresponding author at airoume@uach.cl

Abstract

In this study, we analysed the morphological evolution of a channel segment in the Blanco River in southern Chile that was affected by the Chaitén Volcano eruption occurred in 2008–2009. Through a series of high-resolution satellite images from 2005–2019 that represents the entire pre- and post-eruptive dynamics and land covers, we tracked the geomorphological evolution of a 5.65-km-long river segment using channel form indices and also monitored the vegetation dynamics using object-based image analysis. Discharge record for the Blanco River was also reconstructed to support the analysis of channel morphologic process. In the study, we addressed the following research questions: a) is the Blanco River channel planform still adjusting even 10 years after the eruption and if so, at what magnitude? and b) does the recovered riparian vegetation play a significant role in stabilising the river streambanks and terraces? We found that even 10 years after the eruption, the Blanco River channel planform is still adjusting, showing a simpler and stable channel configuration in the upstream reaches of the valley, where a certain degree of equilibrium appears to have been attained. More complex and dynamic morphologies were observed in the reaches downstream that have to accommodate the arrival of large amounts of freshly eroded sediments. Our analysis showed that the occurrence of competent floods capable of reworking the river channel matches with the geomorphic indices and mark the post-eruption adjustments of the channel. Finally, the in-channel and riparian vegetation does not play a significant role in stabilising the active channel, streambanks, and terraces, reinforcing the recolonization of sedimentary active areas occurring elsewhere in the valley.

Keywords: Channel evolution; Volcanic eruption; Sediment transfer; Vegetation recovery

1. INTRODUCTION

Volcanic eruptions alter nearby river systems, profoundly changing the channel morphology and the patterns of sediment and large wood storage and transport, altogether affecting the successional processes of the riparian communities. Considerable alterations occur immediately after the impact, but the effects on the river dynamics can persist for decades (e.g. Pierson and Major, 2014; Ulloa et al., 2015a).

Explosive volcanic eruptions have the potential to exert some of the most severe eco-hydrogeomorphologic impacts on fluvial ecosystems by depositing large volumes of erodible fragmental material downwind and downstream of volcanoes, filling valley floors, redefining watershed divides, causing widespread damage to hillslopes, riparian and in-channel vegetation by stripping hillslopes of all vegetation, uprooting or burying trees, and toppling, breaking and carbonizing branches, foliage and full trees, and also changing river network patterns, channel size, shape, pattern and channel structure because of the huge deposition of tephra and volcanic debris (Swanson et al., 2013; Pierson and Major, 2014; Ulloa et al., 2015; Juncos et al., 2016; Major et al., 2016). In addition, volcanic eruptions can affect fluvial ecosystems and harm aquatic habitats thus affecting macroinvertebrate and fish communities (Dorava and Milner, 1999). Globally, there is limited information on how local communities recover after large volcanic eruptions (Pierson and Major, 2014). Typically, there is a substantial scientific, political, and media interest when impacts are at their worst, but the interest diminishes during the post-eruption recovery processes, even though this information is crucial for long-term volcanic risk assessment and management (Wilson et al., 2011). Eruptions and associated disturbances are hazardous in their own, but medium to long-term fluvial system adjustments can impose additional hazards on downstream infrastructure and inhabitants (Manville and Wilson, 2004; Kataoka et al., 2009; Manville et al., 2009). Quantifying the resilience to the impacts of explosive eruptions and the subsequent effects on the hydromorphological process-chains and on the island, riparian and hillslopes forests depend to a high degree on the modes and rates at which the altered surrounding landscapes adapt and recover, following a volcanic disturbance (Pierson and Major, 2014).

Most post-eruptive processes are hydrologically and hydraulically driven and can mobilize large volumes of sediments and large wood, i.e., a handful of quantitative studies shows that the highest transport rates measured in rivers had occurred after pyroclastic eruptions (e.g. Major et al., 2016). Reduced infiltration and hydraulically smoother channels on valley floors due to tephra deposits and a decrease in rainfall interception losses owing to the destruction of forests lead to larger flood peaks and faster flood-peak rise times (e.g. Major and Mark, 2006; Pierson and Major, 2014). Increases in discharge and decrease in lag-time time after heavy rains lead to sediment transport dominated by

lahars and high-concentration floods, hence increased sediment yields, and to major stream channel geomorphic changes (Smith, 1991). Sediments inputs from loose and highly erodible deposits along riverbanks and valley floor, and from eroded deposits in hillslopes, increase the volume of material available to transport and cause channel conditions and sediment-transporting processes promoting both greater transport efficiency and higher sediment fluxes (Pierson and Major, 2014). Net accumulation of sediment in streams causes channels to aggrade, which in turn triggers changes in planform channel pattern, channel form (cross-sectional dimensions), channel position within the floodplain and by moving from a single-thread channel pattern to a braided pattern (Gran, 2012). Channel aggradation can also partly or entirely fill the active channels with sediments and large wood and reduce or eliminate channel capacity and increase the magnitude of flooding and can force a river to migrate across an entire valley floor, where infrastructure, agricultural land and forests can be flooded and buried in sediment. (e.g., Lombard et al., 1981). Biological processes such as riparian vegetation encroachment and recruitment on the morphology of river can regulate to a larger extend the landform evolution, by increasing bank strength, bar sedimentation, and enhancing the formation of log-jams, and concave-bank bench deposition (Hickin, 1984; Hupp, 1992; Bertoldi et al., 2011; Osterkamp et al., 2012). Pioneer vegetation that establishes after the disturbance and riparian-species successional patterns, and specially wood vegetation with high stem densities and root system volumes, increases the resistance to erosion in river deposits, enhance bank stability and helps stabilizing the sediments; altogether, increases flow resistance which, in turn, reduces flow velocities during flood events. The interaction between all these processes ultimately causes that channel planform shifts from braided to less dynamic patterns (multithread, anabranching, or even meandering e.g. Gurnell, 2013, Tal et al., 2004; Braudrick et al., 2009; Davies and Gibling, 2011; Gran et al., 2015).

Monitoring the subsequent chain of hydrologic and geomorphic processes has prime societal relevance in a country such as Chile. The country has ca. 99 active volcanoes (from geological evidence on eruptive activity in the last 10 ky), ranking the fifth in a worldwide chart (Global Volcanism Program 2013). However, hydrologic and geomorphic impacts of explosive eruptions on volcanic river systems and the associated patterns of stream channel morphology, including the sediment and massive wood transport evolution were underexplored topics in Chile, until the Chaitén Volcano eruption in 2008–2009 attracted worldwide attention. Studies based on the Chaitén Volcano eruption has enhanced the understanding of short- and medium-term morphological effects of volcanic eruptions on the adjacent river systems. Major et al. (2016) reported that after the great initial flush of sediment into the Blanco River, the sediment supplies declined, the growth of the new delta stabilised by 2011, and the channel bed elevations and planforms recovered to their pre-eruption

conditions within two to seven years, thus concluding that the river achieved a quasi-stable state shortly after the eruption. However, more recent studies report local bank erosions of tens of meters occurring during 2015 (Tonon et al., 2017) and a delayed increase in landslide activity following the Chaitén eruption (Korup et al., 2019). The bank erosions and increased landslide activity are certainly still delivering sediment and large wood into the fluvial network, which indicate that the channel planforms could still be adjusting. In addition, studies have not yet addressed the recovery of islands and floodplain vegetation, which, as stated, play a relevant role in enhancing bank stability and controlling fluvial processes and morphology.

Here, we enlarge our database and used very high-resolution satellite images covering the period 2005 to December 2018 to further expand the analysis of the evolution of the channel planform. In addition, we adopted an object-based image analysis (OBIA) approach to characterise and evaluate the degree of recovery of the channel and floodplain vegetation along the Blanco River channel, with the aim at addressing the following research questions: a) following some indications of stabilization shortly after the eruption, is the channel planform still adjusting even 10 years after the eruption and at what magnitude? and b) has the riparian vegetation recovered to a level at which it can play a significant role in stabilising the streambanks and terraces?

Within this context, the objective of this study was twofold: i) to track the geomorphological evolution of a 5.65-km-long river segment based on the active channel width and braiding, ii) to describe the progressive re-vegetation of the river channel and its dynamics. For this purpose, we undertook a diachronic analysis of a sequence of high-resolution satellite images for the period 2005–2018, which represents the entire pre- and post-eruptive dynamics until now. A reconstruction of the discharge record of the Blanco River was used to support the analysis of channel morphology.

2. STUDY AREA

The selected study area is a channel segment of the Blanco River, which was severely affected by the Chaitén Volcano eruption in 2008. The river is in southern Chile and drains the southern slopes of the Chaitén Volcano (72° 39′ 7″ W, 42° 50′ 1″ S) flowing to the Pacific Ocean through the village of Chaitén (Fig. 1). The basin area at the location of the downstream end of the study segment is 77.2 km^2 with altitudes 10–1545 m above sea level. The Blanco River has a rainfall dominated regime with peak discharges in winter. The valley is glacially incised in a tectonic lineament. The soils have mostly originated from volcanic sediments deposited on the bedrock basement and are quite unstable, which favours creeping and frequent landslides. Alluvial deposits are present in the lowland areas where they are interbedded with pyroclastic deposits (Ulloa et al., 2015a, 2016). Forest belongs to the evergreen forest type (Donoso, 1981), characterised by high species diversity and the presence of

Nothofagus dombeyi, Nothofagus nitida, Nothofagus betuloides, Luma apiculata, Drimys winteri, Eucryphia cordifolia, Weinmannia trichosperma and *Aextoxicon punctatum*.

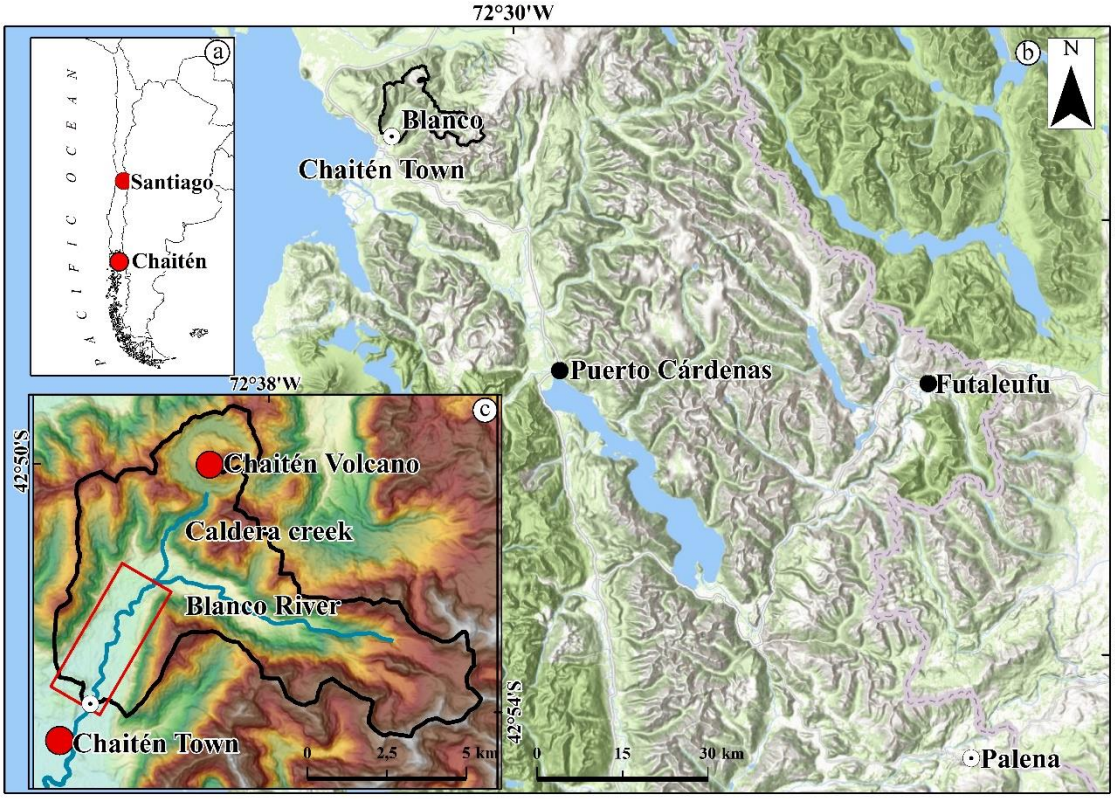

Figure 1. (a) General location of the Chaitén area; (b) general location of the Chaitén town and rainfall (black dot) and discharge (white dot) gauging stations; and (c) the Chaitén town and volcano and the 5.65-km long river segment (within the red rectangle). Images in (a), (b) and (c) from NASA and Aster GDEM 2011.

The volcanic eruption began on 1 May 2008, with an explosive phase that lasted until 11 May 2008 and a long effusive phase spanning from June 2008 to December 2009 (Carn et al., 2009; Lara, 2009; Major and Lara, 2013). Carn et al. (2009), Lara (2009), Major and Lara (2013), and Major et al. (2013) studied the characteristics and different phases of this rhyolite eruption (one of the few of this kind in the past century). Primary disturbance processes included the tephra fall abrasion of foliage from the tree canopy and the deposition of thick volcaniclastic sediments in the surrounding river valleys (Swanson et al., 2013; Major et al., 2016; Ulloa et al., 2016). The small pyroclastic density currents (PDCs) generated during the first phase of the eruption and the additional PDCs after the subsequent partial collapses of the new lava dome affected the lower and upper valleys of the Blanco River (also known as the Chaitén River) (Major et al., 2013; Swanson et al., 2013; Ulloa et al., 2015a,

b, 2016). PDCs severely disturbed the forests mainly at the inner caldera wall and northern flanks of the volcano and travelled downstream the Blanco River, but it neither reached the coastal town of Chaitén nor damaged the local infrastructures (Major et al., 2013; Swanson et al., 2013). Secondary disturbances were mainly driven by the extraordinary sediment flushes generated by the modest rainfall that occurred shortly after the primary phase of the explosive activity (Pierson et al., 2013). Mobilised sediment and channel reworking additionally obliterated the floodplain forests, filled the lower course of the Blanco River channel up to 7 m, buried the city of Chaitén up to 3 m deep, avulsed the river through the town, and created a new delta in the Chaitén Bay (Major et al. 2013, 2016; Pierson et al. 2013; Swanson et al. 2013). The width of the Blanco River almost doubled after the eruption, with significant disturbances occurring during and immediately after the explosive and effusive phases of the Chaitén Volcano (Ulloa et al., 2015a, 2016). In addition to sediment inputs, huge quantities of large wood were introduced into the Blanco river channel where the riparian vegetation was severely affected (Ulloa et al., 2015a, b; Umazano et al., 2014; Tonon et al., 2017). Large wood is highly dynamic, abundant, and form from easily erodible streambanks, with logjams playing a morphological role in modifying the flow direction, downstream flooding, and avulsion (Ulloa et al., 2015a; Umazano et al., 2014; Tonon et al., 2017).

3. METHODS

The morphologic changes of the channel and the riparian forest dynamics from pre- to post-eruptive periods were analysed along a 5.65-km-long river segment, using a sequence of high-resolution images. The length of the study segment was measured in the 2005 pre-eruption image but segment lengths slightly changed along the post-eruptive period. This river segment is in the lower part of the catchment area (Fig. 1, 2), running from the confluence of the Caldera creek with the main channel of the Blanco River to just upstream of the village of Chaitén, and represents the pre- and post-eruptive dynamics (Fig. 2). The upstream limit (altitude of 122 m above the sea level) was defined considering that the Caldera creek connects the caldera with the main channel and that the major morphological changes occurred downstream of this conjunction. The downstream limit (altitude of 10 m above the sea level) was set up to avoid the morphological changes induced by the heavy machinery that was used to artificially widen the channel and protect the streambanks nearby the village. This limit corresponds to the cross section whose time series configuration is presented in Major et al. (2016; top panel in Figure S6 of the supporting information). In addition, to frame an interpretation of the observed changes in the river morphology, a hydrological analysis was undertaken to derive flow data for the Blanco River.

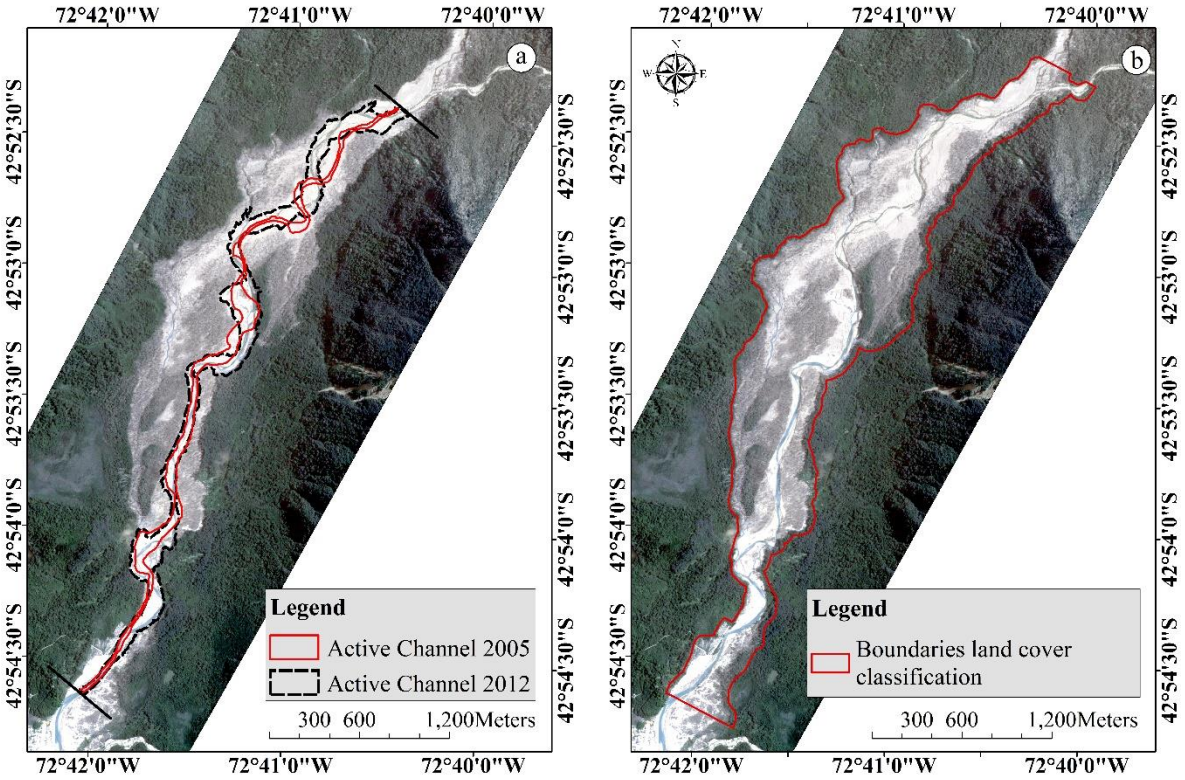

Figure 2**.** a) The active channel for the 2005 and 2012 conditions; b) boundaries of the area for land cover classification and change analysis (red) delineated using the image acquired in 2012 (figure mentioned in Section 3.3).

3.1. Flow series

Hydrological information on the Blanco River catchment area is scarce and is only available for a very short period from January to April 2015, after which the gauging station was destroyed by a series of floods and was never reinstalled. Hence, to support this study from a hydro-climatic point of view, a hydrograph for the Blanco was derived for the period 2005–2018 from the discharges (*Q* hereafter) recorded at the gauging station on the Palena River at Bajo Junta Roselot (12,441 km^2), which is located south of Chaitén, and owns the largest *Q* series near the study area (see Figure 1 for location details). These are daily flows (not instantaneous), and the data is used to provide information about the frequency and 'relative' magnitude of competent flows during the different study periods, and in any case the objective is to perform a quantitative analyses based on flow data.

The best-fitted log-transformation was used between the Palena and the Blanco daily discharges between January and April 2015 (www.dga.cl) (*Q* in the Palena River during the four-month extrapolation period was 40% lower than that for the whole reference period 2005–2018). Daily data for the Blanco River was derived from the general statistical relation between the two rivers and was

213 used to attain a general sense of the behaviour of the river (e.g. mean annual flow) during the study
214 period. It was also used to detect the flood events that could effectively mobilise the river-bed
215 sediments (e.g. number of flow peaks per year) and transform the channel morphology (Fig. 3). This
216 simulated data was not used to characterise the basin's hydrology and the associated flow regime of
217 the river, nor was it used to do subsequent calculations on, for instance, sediment loads. Despite being
218 statistically significant ($N = 106$, $r = 0.65$, $p < 0.01$), the relation between both the real daily flow
219 series (January-April 2015) is highly variable, as typically found in such extrapolation exercises
220 (Gong 2013). Seven direct flow measurements were also done between 2011 and 2018 at the study
221 location, close to the basin outlet. On an average, simulated discharges overestimated the measured
222 flow by 8%, ranging from a 59% overestimation in the case of low flows (i.e. below the annual mean
223 of ca. 8 m^3/s) to a 42% underestimation of the high flows that are above the mean and up to 11 m^3/s
224 (the largest gauged *Q*, 3 March 2012) and are potentially capable of scouring the river-bed sediments;
225 hence, are on the conservative side of the simulated/observed relation. Furthermore, four of the six
226 observed flows lay within the 2 and ½ the simulated values (see Fig. 3). To further check the
227 suitability of the simulated flow series, annual *Q* from both observed (Palena) and simulated flow
228 series (Blanco) that equalled or exceeded 1% (i.e. Q_1 representing high flows) were compared. On an
229 average, $Q_{1\text{-Palena}}$ exceeds 250 times $Q_{1\text{-Blanco}}$, whereas the area ratio between the two basins is only
230 160, confirming the underestimation of the simulated series for high flows. For reference, on an
231 average, Q_1 increased by 60% (from 16.4 to 25.8 m^3/s) in the basin-area ratio method. The runoff was
232 also compared with the rainfall data obtained from the Puerto Cárdenas meteorological station
233 (www.dga.cl), located in the Yelcho River drainage basin south of Chaitén (see Fig. 1 for location
234 details). Both the annual and the daily rainfall-runoff relations were statistically significant, despite
235 the high variability observed between the series (see inset in Fig. 3). As stated above, this hydrological
236 exercise does not intend to give the 'real' hydrology of the Blanco, but to corroborate both the order
237 of magnitude of the simulated discharges and the number of peaks that occurred in the river during
238 the study period.

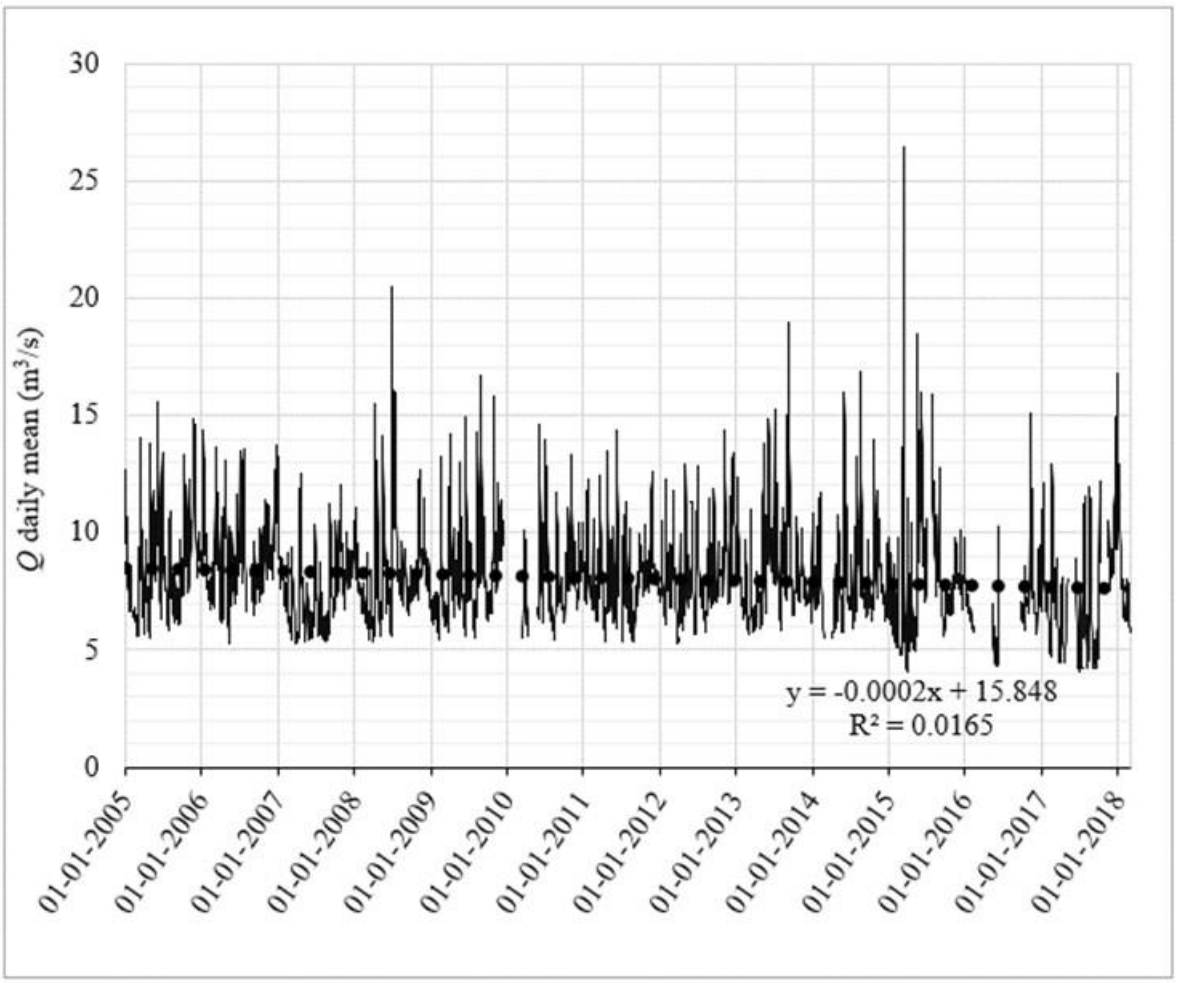

Figure 3. Daily discharge for the Blanco River obtained from records of the neighbouring Palena River (see location details in Fig. 1) by means of log-log transformation procedures (see methods section 3.1. for details). For reference a tendency line is added, showing no statistical trend in the flow series.

3.2. Image analysis and channel characterisation

A multitemporal sequence of eight very high-resolution (VHR) satellite images was used to study the morphological evolution along the river segment. Details about acquisition dates, spaceborn platforms, and ground spatial resolution of each image are summarised in Table 1. The time frame spanned from 2005 (pre-eruption condition) to December 2018. With the exception of the 2005 image, all post-eruption images were acquired during comparable periods of each year regarding both, flow conditions and photosynthetic activity of vegetation. Post-eruption images are all from December to early April, i.e., during the drier months of the southern hemisphere summer, thus trying to target the low flow period. Flows for the dates of these post-eruption images have return periods between 1.1 and 2.5 years, and antecedent precipitation in these occasions was very low (null or up

to 16 mm, from data of the Puerto Cardenas or Futaleufu neighbouring rainfall stations). Although with some degree of uncertainty, we can accept that flow levels are in the same class.

Table 1. Acquisition date, satellites and ground spatial resolution of the satellite images used to perform the morphologic analyses. PAN: Panchromatic; RGB: Red, Green, Blue; NIR: Near Infrared.

Acquisition date	Satellite	Ground spatial resolution (m)	Spectral bands
05-05-2005	QuickBird-2®	0.61/2.4	PAN, RGB, NIR
08-03-2009	WorldView-1®	0.5	PAN
25-01-2012	QuickBird-2®	0.61/2.4	PAN, RGB, NIR
16-12-2013	WorldView-1®	0.5	PAN
15-01-2015	WorldView-3®	0.5/2	PAN, RGB, NIR
01-04-2016	Pléiades®	0.5/2	PAN, RGB, NIR
31-01-2018	GeoEye-1®	0.5/2	PAN, RGB, NIR
02-12-2018	Pléiades®	0.5/2	PAN, RGB, NIR

The first image (dated 2005, 0.61 m panchromatic spatial resolution) permitted to characterise the conditions of the channel and the riparian vegetation before the 2008 Chaitén eruption. We used the moderate-resolution LANDSAT 7® images from 26 October 2006, 3 March 2007, and 2 February 2008, to verify any noticeable changes in the channel geometry and riparian vegetation between the first image (2005) and images from days before the eruption. In the absence of any noticeable changes, the 2005 image was used to represent the pre-eruption condition. One image per date was enough to cover the whole study area; the exception being January 2015 where two images were required to create a unique mosaic using the ArcGIS® Mosaic Dataset. These two images had a partial overlap and were georeferenced using ground control points (GCP) following Batalla et al. (2018). Finally, a geometric correction of the images was performed using a total of 17 GCP established in the 2005 pre-eruption image (2.4 GCP/km^2) and 40–100 GCP (mean 55) in the remaining post-eruption images (7.9 GCP/km^2). Features such as man-made structures (roads, buildings) and topographic (boulders) and vegetation (dead trees) elements were selected (Chuvieco et al., 2010), and a Spline or rubber sheeting transformation (Vericat et al., 2009) was used to test the accuracy of the processing. Mean error varied between 0.01–1.72 m (mean 0.99 m), representing < 4.9% of the median value of the active channel width. Considering the values of resolution of the images and magnitude of the changes observed in the river channel, we assume that the accuracy of the procedure

281 did not significantly affect the results. The lateral boundaries of the active channel were manually
282 digitised in each image. The boundaries were defined as in Ulloa et al. (2015a) as follows: a) in the
283 2005 pre-eruption image the active channel was defined as the area within the lines of the riparian
284 forest on both sides of the channel, and b) in the post-eruption images the active channel of the river
285 was defined as an active channel itself plus "the active floodplain bounded by terraces too high to be
286 inundated when the aerial images were collected". Hence, for the purpose of this paper we define the
287 active channel as the total channel area contained between the riverbanks that limit the adjacent
288 terraces; this definition does not aim at including any process description such as for instance bedload.
289 From the polygon of the active channel for each image, water and sedimentary units were manually
290 mapped. Active channel and wetted areas, and a braiding index proposed by Brice (1964), were then
291 calculated as per Egozi and Ashmore (2008). To calculate the braiding index, we used the information
292 extracted at the cross sections and at the reaches between sections along the 5.65-km-long study
293 segment. Using the 2005 image, we drew the upper cross section (representing the upstream limit of
294 the study segment) perpendicular to the wetted channel and the downstream cross section
295 (representing the downstream limit of the study segment) following the orientation of the first field
296 survey in 2010 of this cross section and maintained the orientation of these two cross sections in the
297 other images. The other cross sections were generated using the ESSA River Bathymetry Toolkit®
298 (RBT) as an ArcGIS® extension (see Batalla et al., 2018), which allow drawing perpendicular cross
299 sections following the channel thalweg at regular intervals. First, the cross sections spaced at ~99 m
300 were defined on the 2005 image (58 cross sections and 57 reaches). The same number of cross
301 sections was demarcated on each of the post-eruption images, although here the spacing was between
302 99 and 101 m due to the changes in channel length and sinuosity that were induced by the cascading
303 effects of the volcanic disturbance.
304
305 **3.3. Land cover classification and change**
306 Remote sensing data can be exploited to effectively assess riparian vegetation temporal changes in
307 spatial patterns. Specifically, high-resolution optical images acquired from different platforms
308 (aircrafts, satellites, and unmanned aerial vehicles) can be coupled with object-based image analysis
309 (OBIA) to characterise riparian vegetation at local to regional scales. Tasks such as species
310 composition (Husson et al., 2016), habitat mapping (Strasser and Lang ,2015), and invasive species
311 mapping (Fernandes et al., 2014) were effectively accomplished using the aforementioned remote
312 sensing methods. In this study, the species composition of vegetation recovering both in the terraces
313 and the active channel were obtained from field observations during January 2015 and 2017 and
314 December 2018. The land cover classification was performed using VHR satellite images acquired

during three different vegetative seasons, one before (2005) and two after the volcanic eruption (2012, using the January 2012 image, and 2019 based on the December 2018 image) (Table 1). The choice of post-eruption images was based on the availability of the NIR band in order to compute vegetation indices such as the Normalized Difference Vegetation Index (NDVI) and because the selected time frame (8 years) guaranteed to detect the recovery of shrubby and arboreal vegetation in the short-medium term. The following classes were identified: forest (tree canopy cover > 80%), dense vegetation (shrubs and herbs cover > 60%), sparse vegetation (shrubs and herbs cover between 10-59%), bare soil (sand, gravel, rocks and vegetation cover < 10%), and water. The pre-eruption image was classified through on-screen visual interpretation using Google Earth®. Post-eruption multispectral images were first up scaled to the resolution of the panchromatic band using the Gram-Schmidt pan-sharpening technique (Laben and Brower, 2000). The Automated and Robust Open-Source Image Co-Registration Software (AROSICS®) (Scheffler et al., 2017) was employed to correct the local geometric misregistrations between the images from 2012 and 2019. Multi-resolution image segmentation and object-based classification procedure were performed using original pan-sharpened spectral bands (RGB, NIR) and NDVI through Trimble eCognition® software. Image objects were classified using the support vector machines (SVMs) algorithm with the radial basis function kernel (Huang et al., 2002; Kavzoglu and Colkesen, 2009). Classification accuracy was performed on post-eruption images using 100 randomly distributed points stratified by the five land cover classes for each map. No accuracy assessment was performed on the 2005 image because it was assumed to be accurately classified during manual digitisation. Land cover changes were assessed within different areas of interest (AOI): 1) the whole disturbed area along the study segment of the Blanco River that was clearly recognisable in the 2012 image (Figure 2b) and which was slightly expanded using a 20 m positive buffer resulting in an overall extension of 310 ha; 2) the pre- and post-eruption active channels relative to 2005, 2012 and 2019 vegetative seasons; 3) the areas where the width of the active channel increased in the vegetative season of 2019, i.e. not belonging to the active channel in 2012, with an extension of 26 ha. This latter AOI was delineated in order to evaluate the influence of different vegetation cover types (forest, dense vegetation, sparse vegetation) on the morphological evolution of the active channel and were obtained from the spatial difference between the active channel polygons of the vegetative seasons of 2012 and 2019, respectively.

4. RESULTS

4.1. Hydrology

Table 2 presents the statistics that characterise the hydrology of the Blanco River for the study period 2005–2018. Q_{mean} is 8.06 m^3/s with a low coefficient of variation between the years (6.5%), whereas

$Q50$ had a somewhat lower performance (7.7 m^3/s). Both daily and annual Q_{mean} show a declining trend, without any statistical significance (Fig. 3). The river never dries out, and the minimum flows remain well above 4 m^3/s.

Table 2. Summary of the hydrology of the Blanco River during the study period. Flow data is derived from Q series in the neighbouring Palena River after statistical procedures described in section 3.1. and illustrated in figures 3 and 4.

	Q_{mean}	$Q_{mean\text{-}normalized}$	Q_{50}[1]	Q_1[2]	Q_{max}	n. $Q_{peak}>Q_1$
2005	8.57	1.07	-	-	15.6	3
2006	8.86	1.10	-	-	14.3	0
2007	7.51	0.94	-	-	13.2	0
2008	8.30	1.03	-	-	20.5	7[a]
2009	8.31	1.04	-	-	16.7	7
2010	7.96	0.99	-	-	14.6	1
2011	8.07	1.00	-	-	14.4	0
2012	8.35	1.04	-	-	14.4	0
2013	8.33	1.04	-	-	18.9	6
2014	8.11	1.01	-	-	16.9	4
2015	7.80	0.97	-	-	26.4	8
2016	6.99	0.87	-	-	15.1	1
2017	7.18	0.89	-	-	16.8	2
2018	8.43	1.05	-	-	17.9	3
2005-2018	8.03	-	7.73	14.5[b]	26.4	42

[1] Discharge equalled or exceeded 50% of the time (median discharge) (Fig. 4).
[2] Discharge equalled or exceeded 1% of the time (infrequent high discharge) (Fig. 4).
[a] Year 2008 experienced seven days of competent discharges of which six occurred after the eruption (Fig. 3).
[b] Competent Q capable to fully mobilized $>D_{84}$ (114 mm) of the river-bed material according to bedload samples taken in the lowermost monitoring section of the river in March 2012 (see Fig.1 for locations details).

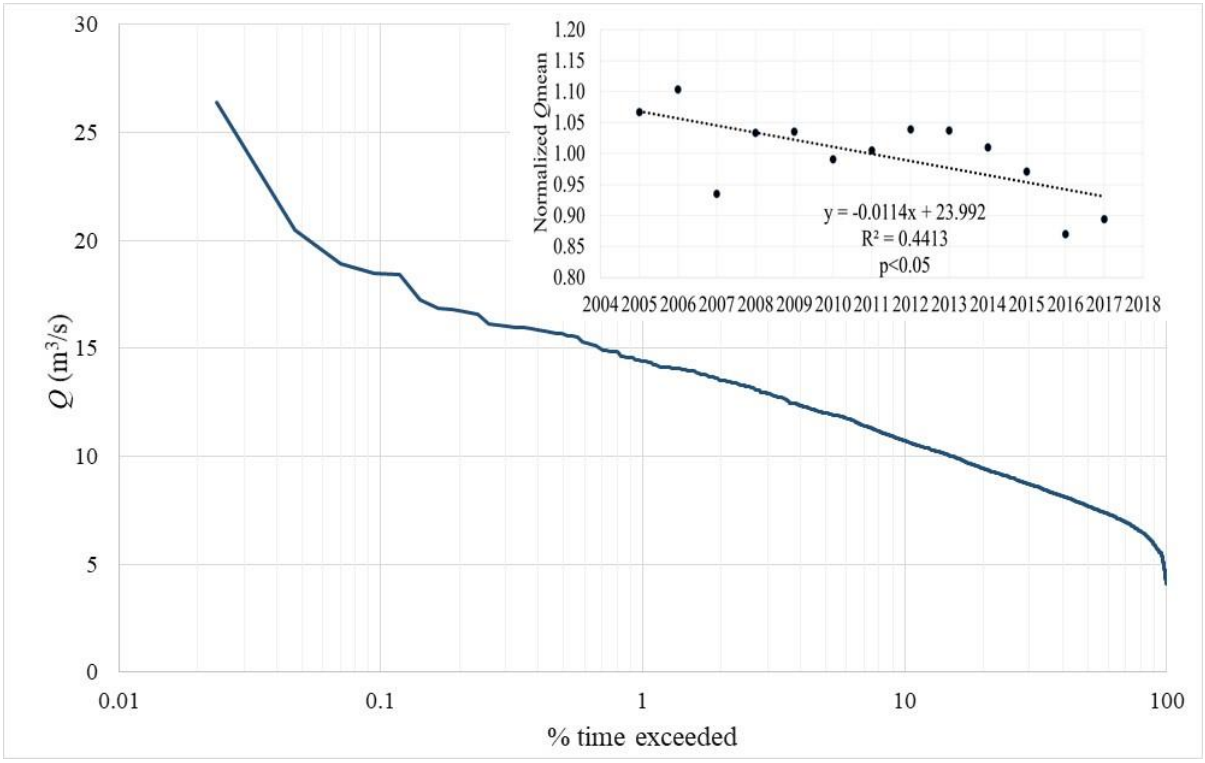

Figure 4. Flow duration curve of the River Blanco along the study period 2005-2018 from daily data. The inset illustrates the evolution of the mean annual discharge in relative terms i.e. over the mean discharge of the whole study period).

Of special geomorphic relevance was 2015, when despite Q_{mean} being not particularly high and close to the mean flow of the period (97% of the $Q_{mean\ 2005\text{-}2018}$), the Blanco River still experienced the largest number of days with high flows (floods). In total, eight days recorded discharges larger than 15 m^3/s (Q_1 from the Flow Duration Curve, Figure 4). Based on direct bedload samples taken between 2008 and 2013 at the lowermost section of the river (supplementary material in Major et al., 2016), we consider Q >12 m^3/s competent enough to mobilise most of the bed-material (>D_{84} of the river-bed grain-size, i.e. 113 mm); hence hypothetically capable of reworking river-bed configuration. In particular, near-full mobility of bed-material was observed during sampling performed on March 5th, 2012 under 11.9 m^3/s that yielded a median bedload particle size of 90 mm and a D_{84} of 114 mm. Q_{max} of the whole study period also occurred in 2015 reaching 26.4 m^3/s. The mean of Q_{max} is 16.8 m^3/s with a moderate coefficient of variation of 21%. A total of 42 *competent* floods occurred during the study period (Table 3), with several years not displaying competent flows. However, it should be remembered that the flow data was derived from the River Palena and absolute Q values in the Blanco were not available.

4.2. Changes in the channel

By 8 March 2009, i.e. shortly after being hit by the second and last PDC generated by a partial collapse of the new lava dome (Major et al., 2016), the active channel area and width increased by 2.6 times its pre-eruption dimensions (Table 3). The active channel area increased from 220,000 to 577,000 m^2 and the median and mean values of the channel width increased from 35.2 and 39.5 m to 88.4 and 102.3 m, respectively. The eruption increased the maximum active channel width from 88.2 to 305.4 m. The wetted channel area measured on 8 March 2009 is the largest of the different studied dates (see Table 3). As all the images represent relatively similar flow conditions, this could be because the channel was still filled with sediments after the eruption and the water was flowing in a less channelized river, occupying most of the channel bottom.

Table 3. Active and wetted channel areas (m^2) and widths (m) and braiding index for the different time intervals.

	05-05-2005	**08-03-2009**	**25-01-2012**	**16-12-2013**	**15-01-2015**	**01-04-2016**	**31-01-2018**	**02-12-2018**
Active channel area (m^2)	219.938	576.809	483.807	561.825	589.095	672.843	720.003	737.686
Median active channel width (m)	35.2	88.4	73.0	80.1	91.7	103.3	115.8	115.0
Maximum active channel width (m)	88.2	305.4	219.0	256.4	249.1	267.3	272.2	250.4
Wetted channel area (m^2)	179.711	337.375	88.162	117.702	155.775	113.078	126.242	175.319
Median wetted channel width (m)	23.1	51	13.5	18.4	19.1	19.1	21.8	28.5
Maximum wetted channel width (m)	67.1	191	42.4	64.6	64.6	43.9	57.7	58.8
Braiding Index (D)[a]	1.07	1.79	1.33	1.28	1.19	1.41	1.34	1.62

[a] $Bl_{ti} = \langle N_L \rangle$ per XS (-), $Bl_{t2} = \langle N_L \rangle$ per reach, $Bl_{t3} = \langle N_L \rangle$ per XS (-) (after Howard et al., 1970 and Hong and Davies, 1979).

During the first three years of the post-eruption period (2009, 2010, and 2011), there was a noticeable reduction in the active channel area and width; by January 2012 the former was 483,807 m^2 and the latter recorded 73.0 and 82.3 m for median and mean values, respectively. The maximum channel

401 width of the study segment reached 219 m, i.e. nearly 72% of the maximum width from that recorded
402 just after the eruption. However, after 2012 and 2013, the active channel area and width as well as
403 the maximum channel width increased again, probably due to the 2013 floods that damaged roads
404 and bridges in the Chaitén area (Inostroza, 2014). Moreover, after these two dates, December 2012
405 and June–July 2013, an expansion trend in the active channel area and width was recorded, which
406 lasted until the end of the study period, with a significant increase during 2015 (see the changes
407 between the 15 January 2015 and 1 April 2016 data, Table 3).
408 The reach channel widths were statistically different between the 2005 (pre-eruption) and the 8 March
409 2009 (post-eruption) conditions (nonparametric Wilcoxon–Mann–Whitney (MW) test, *p*-value = 0.0;
410 Fig. 5). On the other hand, the reach channel widths during the different post-eruption periods were
411 also statistically different (nonparametric Kruskal–Wallis (KW) test, *p*-value = 0.0; Fig. 5). Further
412 analyses indicate that the channel widths during the first six years after the eruption (images from 8
413 March 2009 to 15 January 2015; KW test, *p*-value = 0.08, data not shown) and the following four
414 post-eruption years (images from 1 April 2016 to 2 December 2018; KW test, *p*-value = 0.16, data
415 not shown) were statistically similar, but between the two groups they were statistically different
416 (MW test, *p*-value = 0.0, data not shown). Median of the widths for the first six years and the
417 following four years were 81 and 109 m, respectively.
418
419
420

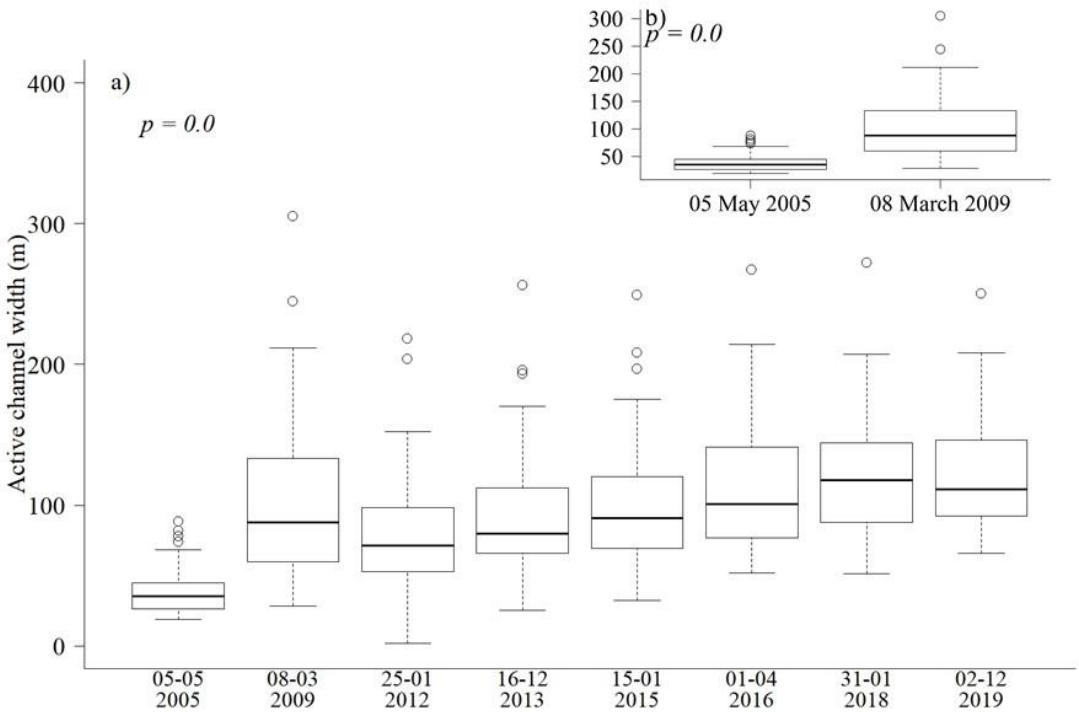

Figure 5. Boxplots of active channel width (m) for different time periods: a) from 8 March 2009 to 2 December 2018, and b) 5 May 2005 (pre-eruption) and 8 March 2009 (post-eruption). The bottom and top of the box indicate the first and third quartiles, respectively, the black line inside the box is the median value, and the whiskers show the largest value within 1.5*interquartile range from third quartile and the minimum value, whereas circles are the outliers. In a) and b), *p* values using the Kruskal–Wallis and Mann-Whitney nonparametric tests, respectively.

Although the eruption affected almost the entire study segment, the initial channel widening was concentrated mainly between cross sections 1 and 16, i.e. in the 1.5-km-long upstream portion of the study segment (Fig. 6a). Here, the channel widening exceeded 100 m at many of the cross sections and more than 200 m at the cross sections 15 and 16. By 25 January 2012, the channel became narrower than it was on 8 March 2009, and most of these changes were concentrated between the cross sections 8 and 29, especially cross section 15, which experienced the largest widening during the previous period (Fig. 6b). From 25 January 2012 to 15 January 2015, the channel experienced a localised widening of up to 80 m (Fig 6c, d). Additional changes occurred from 2015 to the end of the study period (images from 15 January 2015 to 2 December 2018), where the channel widened especially at the downstream end of the study segment, i.e. downstream from the cross section 36 (Fig. 6e, f, g).

Index D (Howard et al. 1970; Hong and Davies 1979), increased by ~67% (Table 3) was immediately

441 altered after the eruption and in the following years ranged 11–44% higher than the pre-eruption
442 condition, showing a significant increase during the last part of the study period (i.e., December
443 2018).

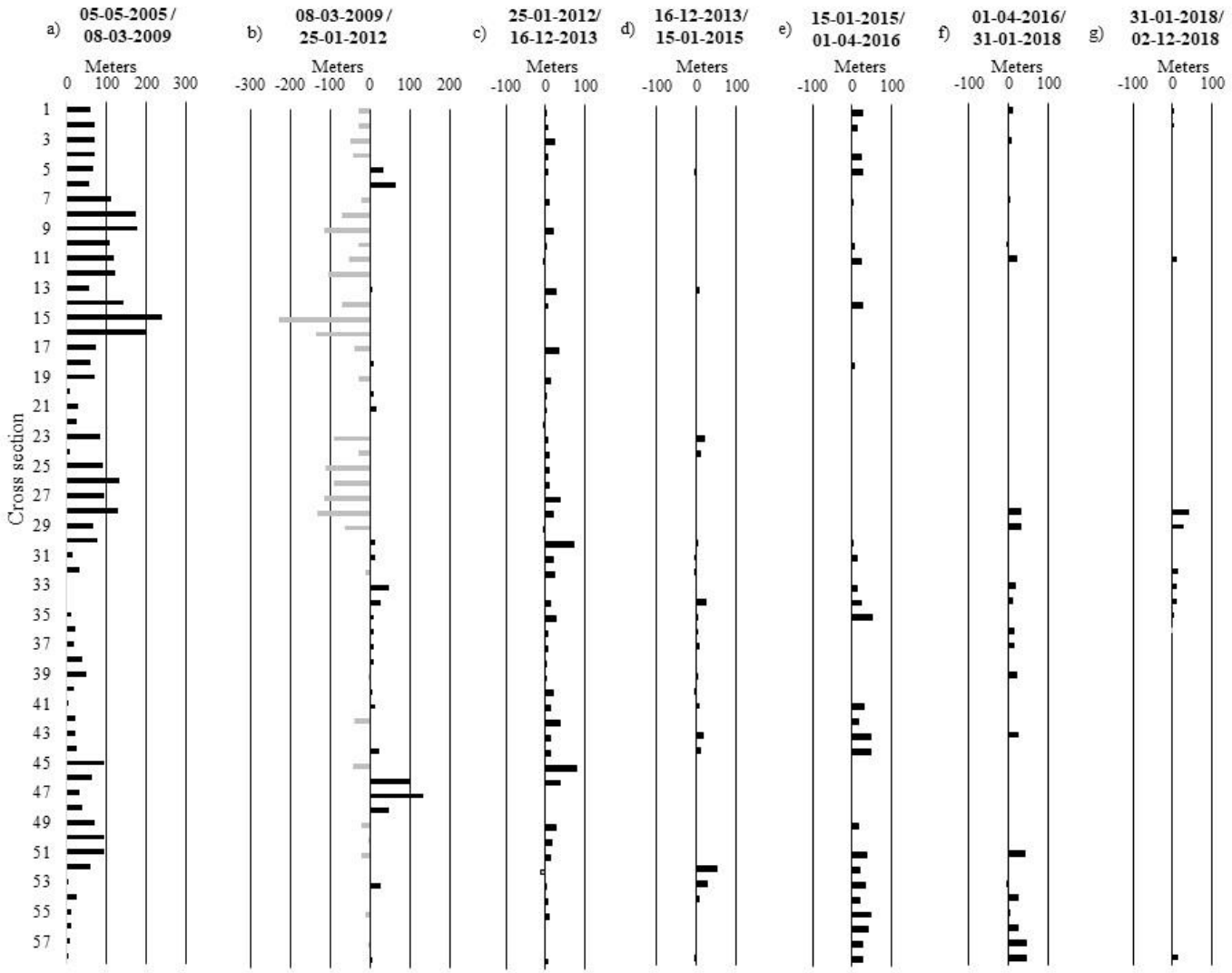

444

445 Figure 6. Changes in the active channel width along different cross-sections of the study segment and between consecutive time study periods.

Figure 7 shows the spatial and temporal evolution of the braiding intensity index based on the values computed at each cross-section (see Methods and Table 3) using a heat map. Values vary from 1 to 5, 5 being the maximum number of channels accounted for in the segment. The heat map indicates that the Blanco River had a very simple channel (almost a single thread) along the study segment before the eruption. Immediately after the eruption, the river evolved to a more complex channel pattern, especially in the upstream reaches, and also in some of the middle and downstream sub-segments. Although most of the reaches had one or two channels, observed dominant process was incision and, if the valley configuration permitted, widening. Several sub-segments showing evident changes were identified: i) three reaches at the upstream end of the study segment (with an extension of ~300 m) showed higher number of channels (3–5), but they returned to a single-thread pattern soon after; ii) further downstream, a sub-segment of ~1.1 km (at distances of 2.5 and 3.6 km from the upstream end) initially showed a complex pattern (2–4 channels) and kept this complex pattern along time until the end of the study period, when the index was again reduced to 1; and (iii) towards the downstream end of the study segment, the eruption generated a more complex channel pattern (the index increased up to 4); in this ~1.1-km-long sub-segment (at distances of 4.4 and 5.5 km from the upstream end), index showed values between 1 and 3 with most prominent changes appearing during the last years of the study, when the index increased even further (up to 5). In general, after the eruption, the channel complexity was higher, but later the channel became seemingly stable in the upstream end, with the lowermost end becoming increasingly active and complex with time.

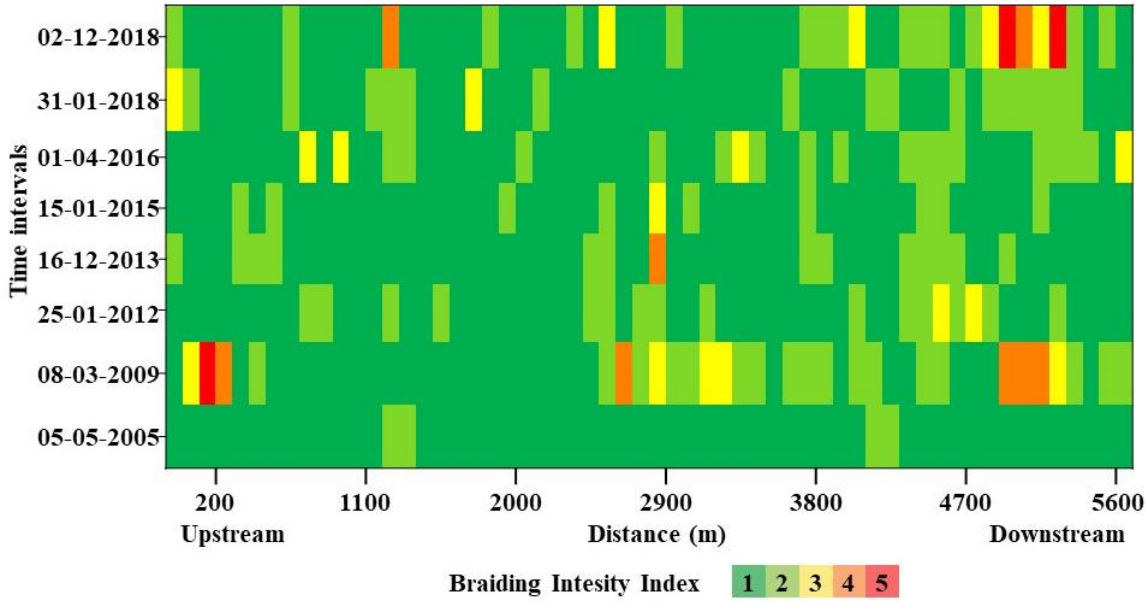

Figure 7. Heat map of the Braiding Index of the Blanco River (see Table 3 for details). Flow direction is from left to right.

Figure 8 highlights the changes in selected river sub-segments during the study period described as follows: (i) before the eruption, the Blanco River featured a simple channel pattern, more wandering in the upper sub-segments and straighter in the downstream ones; (ii) immediately after the eruption (see the 8 March 2019 image) the channel widened in the three sub-segments, although it is not easy to clearly identify the channels as the river flow was covering most of the channel bottom; (iii) by January 2012, three years after the eruption, the active channel narrowed, especially in the upstream and middle sub-segments, whereas a clear straight channel was still observed in the downstream sub-segment. In the two upstream sub-segments, along the right streambank, the abandonment of morphological units was evident just after the eruption; they were part of the active channel and now have become terraces well elevated above the thalweg; (iv) since 2012, the channel widened again, and these changes were concentrated mainly in the downstream sub-segments as illustrated in Fig. 6; and, finally, (v) 10-y after the eruption, the river is gradually moving to more simple pattern, despite planimetric differences with the pre-eruption conditions are very visible, showing a more stable channel configuration in the upstream sub-segments, whereas more complex and dynamic morphologies still persist in the downstream ones. In addition, two facts stand out: (a) the permanent shift in the channel edge along the entire post-eruption period and (b) the preservation of a relatively simple channel pattern in localised areas with more than three channels, as shown in the heat map (Fig. 7).

4.3. Land cover analysis

The overall classification accuracy varied between 82.9% and 80.2% and the Cohen's K statistic varied between 0.77 and 0.73 for the maps of 2012 and 2019, respectively. Between the vegetative seasons of 2005 and 2012, the whole disturbed area was characterized by a strong decrease of forest cover (84.8%) in favour of bare soil, sparse vegetation, and dense vegetation classes that increased by 39.3%, 31.4%, and 17.4%, respectively (Figure 9, Table 4). Minor changes occurred between the vegetative seasons of 2012 and 2019 when the forest cover increased by 12.7% (39 ha) mostly at the detriment of dense vegetation cover (Table 4, Table S1). Considering the changes occurred at the active channel (Figure 10), vegetation cover (forest, dense and sparse vegetation) between 2005 and 2012 decreased by 62.6% in favour of bare soil areas (+70%) whereas its changes between 2012 and 2019 were not significant. Regarding the areas where the active channel width increased in the vegetative season of 2019 compared to that of 2012, the main classes were bare soil (54%) and sparse vegetation (26%) in 2012 and bare soil (71%) and water (14%) in 2019 (Table 5, Table S2). The small vegetated areas observed in 2012 were all affected by the widening of the active channel: sparse vegetation decreased by 17.7%, dense vegetation decreased by 11.5% and forest decreased by 1.5% (Table 5).

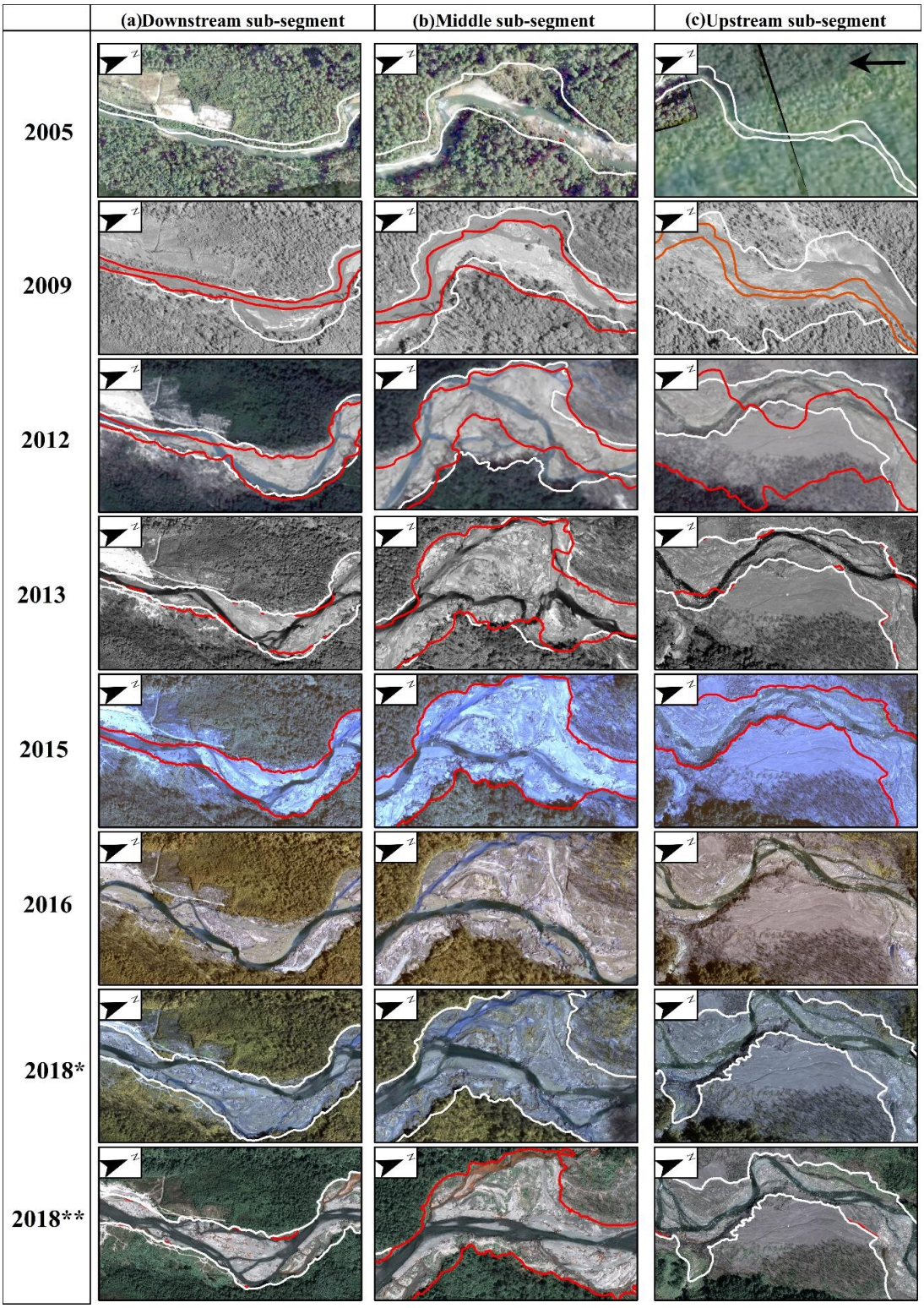

Figure 8. Morphologic evolution of the active channel in selected sub-segments along the study segment. Flow direction is from right to left (see black arrow on top). For period 2005, white line indicates the limit of the active channel. For following periods, white line is the limit of active channel for the period and red line the limit of active channel of previous period. * image January 2018; **

image December 2018.

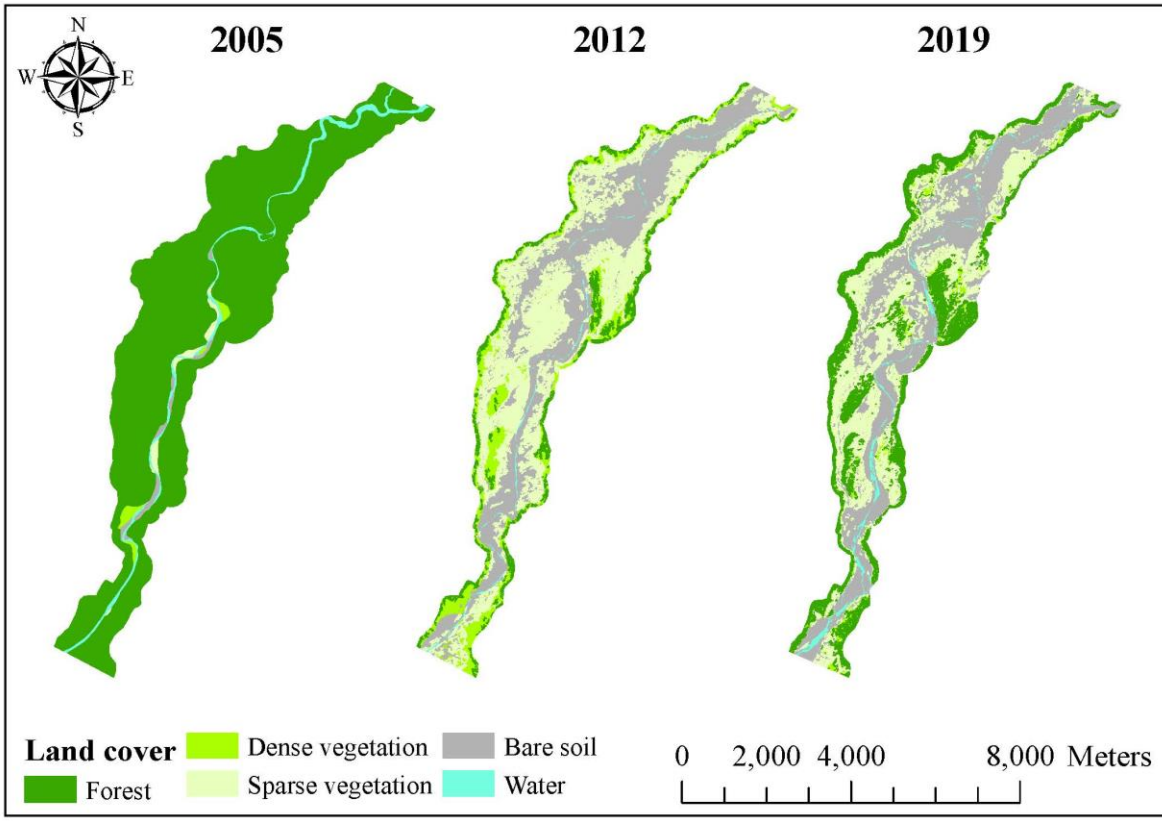

Figure 9. Land cover maps of pre- and post-eruption vegetative seasons of the affected area surrounding the fluvial study segment of the Blanco River in 2005, 2012, and 2019.

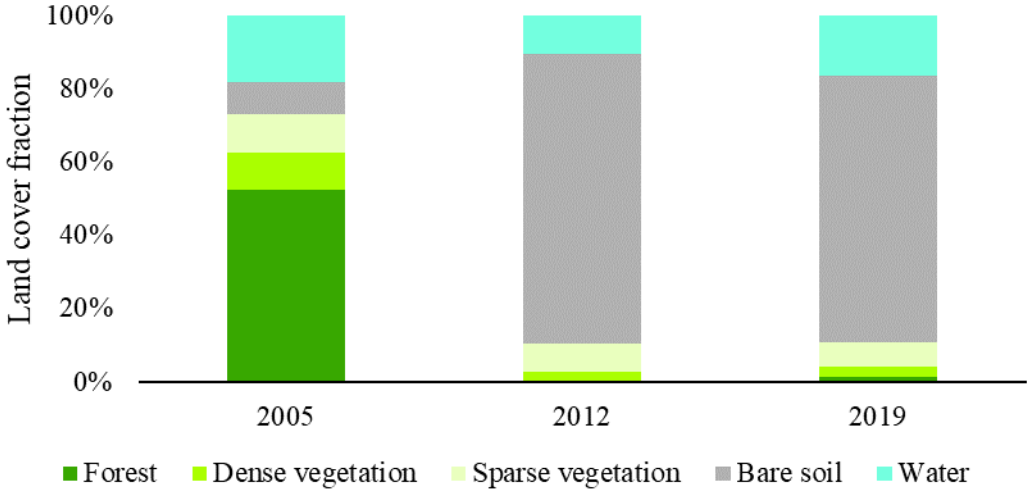

Figure 10. Relative land cover within active channels in the vegetative seasons of 2005, 2012 and 2019.

Table 4. Land cover in different vegetative seasons (2005, 2012, and 2019) and land cover changes occurred between periods 2005-2012 and 2012-2019. Absolute change refers to the extent of those areas that changed class in the following period.

	2005		2012		2019		2005-2012		2012-2019	
Land cover class	**Area (ha)**	**Area (%)**	**Area (ha)**	**Area (%)**	**Area (ha)**	**Area (%)**	**Absolute change (ha)**	**Relative change (%)**	**Absolute change (ha)**	**Relative change (%)**
Forest	281.81	90.95	18.97	6.12	58.26	18.80	-262.84	-84.83	39.29	12.68
Dense vegetation	3.31	1.07	57.28	18.49	31.12	10.04	53.97	17.42	-26.16	-8.44
Sparse vegetation	3.92	1.26	101.26	32.68	80.45	25.97	97.66	31.42	-20.81	-6.72
Bare soil	3.78	1.22	125.46	40.49	125.35	40.46	125.08	39.27	-0.11	-0.04
Water	17.03	5.50	6.88	2.22	14.65	4.73	-8.97	-3.28	7.77	2.51

Table 5. Land cover changes occurred in areas where the active channel was wider in the vegetative season of 2019 compared to that of 2012. Absolute change refers to the extent of those areas that changed class in the following period.

Land cover class	2012		2019		2012 - 2019	
	Area (ha)	Area (%)	Area (ha)	Area (%)	Absolute change (ha)	Relative change (%)
Forest	1.24	4.79	0.85	3.27	-0.39	-1.51
Dense vegetation	3.85	14.85	0.86	3.30	-2.99	-11.54
Sparse vegetation	6.73	25.97	2.15	8.29	-4.58	-17.68
Bare soil	13.89	53.57	18.37	70.88	4.49	17.31
Water	0.22	0.83	3.70	14.26	3.48	13.43

5. DISCUSSION

5.1. Morphology

During the 10-day explosive phase of the 2008–2009 eruption of the Chaitén Volcano, the neighbouring watersheds were covered with > 1 m of tephra deposits. In addition, the pyroclastic flows delivered additional sediments and the rainfalls that shortly followed the major phase of explosive activity triggered extraordinary sediment flushes aggrading the valley bottom of the Blanco River, causing the river to avulse through the Chaitén town (Pierson et al., 2013; Swanson et al., 2013; Major et al., 2016). The eruption caused significant modifications in the Blanco River channel morphology, affecting the whole valley bottom; Ulloa et al. (2015) reported channel widening of up to 3.5 times, increase in the channel sinuosity, and changes from single to multithread channel patterns in specific river reaches between 2005 (pre-eruption) and 2009 (post-eruption). These were certainly associated with the great flush of sediments, reported by Pierson et al. (2013) and Major et al. (2016), which occurred during the days and weeks following the eruption. However, Ulloa et al. (2015) indicated that by 2012, i.e. a little less than four years after the massive sediment loading, the channel planform was recovering some pre-eruption characteristics, while Major et al. (2016) found that by March of the same year, the river had nearly re-established the pre-eruption bed level. These facts suggest an apparently fast recovery, considering that it typically takes one to two decades for a river to restore its pre-eruption morphodynamics (e.g. Gran and Montgomery, 2005; Major and Mark, 2006; Gran, 2012; Pierson et al., 2011; Pierson and Major, 2014). However, there are some

547 exceptions, e.g. the River Opak recovered its pre-eruption conditions in less than five years after the
548 Merapi eruption in 2010 (Gob et al., 2016).
549 By 8 March 2009 (i.e. less than one year after the onset of the eruption), the active channel area and
550 width of the study segment had significantly increased by 2.6 times the pre-eruption condition, with
551 the channel widening concentrated mainly in the 1.5-km-long upstream part of the study segment
552 (Fig. 6a). Comparing the pre- and post-eruption conditions, channel width increments of the same
553 order of magnitude were reported for this river by Ulloa et al. (2015), but for a different river segment.
554 The wetted channel area measured on 8 March 2009 is by far the largest among those in the different
555 studied time intervals. We assume that it is not related to floods (no rainfall was recorded since mid-
556 February 2009 (www.dga.cl) at Puerto Cardenas, a rainfall station 36 km from Chaitén, see location
557 on Fig. 1) but to the huge amount of sediments that still filled the channel after the eruption, which
558 caused the water to flow in a less confined channel, occupying most of the channel bottom.
559 During the three following years, i.e. 2009–2011, a reduction was observed both in the active channel
560 area and its width. By the end of January 2012, the channel was already narrower than in March 2009,
561 and most of the observed changes were concentrated in the upstream 2.9 km of the study segment i.e.
562 the channel portion that experienced the highest post-eruption widening (Fig. 6b). Generalized
563 channel incision and the subsequent abandonment of previously active sedimentary areas explain the
564 reduction of both active area and width (see Fig. 8 for details). Throughout the next two years (i.e.
565 2012 and 2013) the active channel area and width, as well as the maximum channel width, increased
566 again following the floods that occurred mainly in 2013 (see Table 3 and Fig. 6). By 2013, the channel
567 bed elevations recovered to their pre-eruption conditions (see Major et al., 2016; top panel in Figure
568 S6 of the supporting information) thus generalized incisions did not seem to further occur. This
569 assumption is also supported by the energy limit imposed by the sea level.
570 Further morphological planform changes were also observed from 2015 to the end of the study period
571 (images from 15 January 2015 to 2 December 2018), when the channel significantly widened
572 especially in the downstream 2 km of the study segment (Fig. 6e, f, g). Of special geomorphic
573 relevance was 2015 when the maximum Q of the whole study period occurred and the river
574 experienced eight days of high flows (see Fig. 3) that were competent enough to mobilise most of the
575 bed-material and hypothetically capable of reworking the whole river channel configuration.
576 Overall, the eruption changed the channel planform along the entire study segment, which became
577 wider, braided, and more sinuous than pre-eruption i.e. the channel became more complex (see the
578 time trend of the channel morphological indices in Table 3). With time, the channel has become
579 seemingly more stable in the upstream end of the segment, although it is still showing high instability
580 and complexity in the lowermost end. We interpret this as the consequence of the sediment wave

propagation along the channel that still requires at-a-reach adjustment in terms of geometry and sediment budget there. This leaves relatively a simple and stable channel configuration upstream where a certain degree of equilibrium has been attained, whereas more complex and dynamic morphologies develop in reaches downstream, where the river has not adjusted to the arrival of large amounts of freshly eroded and transported sediments yet.

Sediment supply declined despite the high flush of sediments in the days and weeks that followed the May 2008 explosive activity (Pierson et al., 2013; Major et al., 2016), as shown in the time series of the Blanco River delta growth and bed load flux in Major et al. (2016). However, pre-eruption terraces filled with pyroclastic erodible sediments continue to provide a large amount of material to the channel. The channel is widening and eroding these unstable banks.

5.2. Vegetation

Different disturbances triggered by the volcanic eruption of 2008-2009 affected the biological components of the Blanco River, such as air-fall tephra, floodplain deposition of remobilized tephra, and pyroclastic-flow zones (Swanson et al., 2013). The high severity of the disturbance is highlighted by the noticeable forest cover loss occurred between 2005 and 2012 in the area surrounding the fluvial corridor of the study segment. The moderate increase of forest cover occurred between 2012 and 2019 was mainly due to the recovery of dense patches of damaged shrubs and trees which responded through agamic regeneration. Survived individuals of some species such as *Drimys winteri*, *Amomyrtus luma* and *Weinmannia trichosperma* partially recovered through crown and basal re-sprouting after the loss of foliage and the breakage of branches and trunks as observed also by Swanson et al. (2013). Sparse vegetation was frequently associated with lying deadwood and, although it was initially formed only by herbaceous species (e.g. *Gunnera tinctoria*) and ferns, lately also by tree seedlings of shade-intolerant *Nothofagus* species (e.g. *N. dombeyi* and *N. Nitida*). These latter are known to have the ability to regenerate after stand-replacing disturbances and in suboptimal edaphic conditions (Veblen and Alaback, 1996; Veblen et al., 1996; Pollmann and Veblen, 2004). Land cover changes occurred at the active channels between 2012 and 2019 (Tables 5 and 6) indicated that about 80% of the areas where the active channel width increased were solely covered by bare soil and sparse vegetation. On the contrary, the areas surrounding the active channel with developed vegetation favoured its stabilisation. Forests on these latter areas were affected by low and moderate severity and recovered faster than those affected by high severity due to the lower percentage of tree mortality.However, given the huge proportion of bare soil still occurring in the vegetative season of 2019 (Figure 10), vegetation recovery at the active channel appeared to be highly delayed. In this sense, the river has been very active in reworking its own deposits, wandering from one bank to the

other during lower flows and occupying the entire active channel during floods, thus reducing the chances for establishment of vegetation that could potentially facilitate the stabilisation. During the vegetative season of 2019 (Table 5, Fig. 9), the overall potential of vegetation to stabilize the stream bank was still limited since two-thirds of the disturbed areas surrounding the fluvial corridor of the study segment were formed by bare soil and sparse vegetation. This favoured the erosion of unstable stream banks composed mainly of pyroclastic, low-density, lithic-rich, and loose gravelly sand where herbaceous species such as *Gunnera tinctoria* were abundant but unable to increase bank strength.

6. CONCLUSIONS

The objective of the study was to carry out a diachronic analysis of the geomorphic evolution of the Blanco River, after the Chaitén Volcano eruption in 2008. A series of high-resolution satellite images representing the entire pre- and post-eruptive dynamics (2005–2019) were analysed. The analysis was supported by hydrological data extrapolated from neighbouring catchments for which discharge series were available. The main conclusions of the paper are summarised as follows:

1) Ten years after the eruption of the Chaitén Volcano, the Blanco River channel planform is still adjusting, showing a simple and stable channel configuration in the upstream segment of the valley, where a certain degree of equilibrium appears to have been attained, whereas more complex and dynamic morphologies are still observed in the reaches downstream, where the river is still adjusting to the arrival of large amount of freshly eroded sediments.

2) The occurrence of competent floods capable of reworking the river channel matches with the evolution of the geomorphic index (braiding) used here and mark the channel post-eruption adjustments.

3) Finally, the in-channel and riparian vegetation has not yet recovered to a level where it could play a significant role in stabilising the active channel, streambanks, and terraces, despite the recolonization of active sedimentary areas observed elsewhere in the valley.

Overall, evaluating the decadal evolution of post-eruption responses of channel corridors, as we have done here with Blanco (or Chaitén) River, provides insights to avoid underestimating the time required to reach a new equilibrium condition, whereas at the same time add crucial information for the continuous update of river risk management plans in areas recurrently affected by this catastrophic events.

Acknowledgements

This research was developed within the frame of the project FONDECYT 1170413 funded by the Chilean Government. Authors acknowledge the support of the Economy and Knowledge Department

of the Catalan Government through the Fluvial Dynamics Research Group (RIUS) SGR017-459. Authors thank Damià Vericat for revising the first version of this manuscript.

Conflict of Interest

The authors declare no conflict of interest.

Data Availability

Data will be available upon request to the main author.

REFERENCES

Alfano, F., Bonadonna, C., Volentik, A.C.M., Connor, C.B., Watt, S.F.L., Pyle, D.M., Connor, L.J., 2011. Tephra stratigraphy and eruptive volume of the May, 2008, Chaitén eruption, Chile. Bulletin of Volcanology, 73 (5), 613–630.

Batalla, R.J., Iroumé, A., Hernández, M., Llena, M., Mazzorana, B., Vericat, D., 2018. Recent geomorphological evolution of a natural river channel in a Mediterranean Chilean basin. Geomorphology, 303, 322-337.

Brice, J.C., 1964. Channel Patterns and Terraces of the Loup Rivers in Nebraska. Geological Survey Professional Paper 422-D.

Carn, S.A., Pallister, J.S., Lara, L., Ewert, J.W., Watt, S., Prata, A.J., Thomas, R.J., Villarosa, G., 2009. The unexpected awakening of Chaitén Volcano, Chile. Eos, Transactions, American Geophysical Union, 90 (24), 205–206.

Chuvieco, E., 2016. Fundamentals of Satellite Remote Sensing: An Environmental Approach. Second edition. Taylor and Francis, USA (468 p).

Donoso, C., 1981. Tipos forestales de los bosques nativos de Chile. Documento de Trabajo Nº 38. Investigación y Desarrollo Forestal (CONAF, PNUD-FAO). FAO Chile, Santiago de Chile.

Egozi, R., Ashmore, P., 2008. Defining and measuring braiding intensity. Earth Surf. Process. Landf., 33, 2121–2138.

Global Volcanism Program, 2013. Volcanoes of the World, v. 4.7.6. Venzke, E (ed.). Smithsonian Institution. Downloaded 01 Apr 2019.

Gob, F., Gautier, E., Virmoux, C., Grancher, D., Tamisier, V., Primanda, K.W., Wibowo, S.B., Sarrazin, C., de Belizal, E., Ville, A., Lavigne, F., 2016. River responses to the 2010 major eruption of the Merapi volcano, central Java, Indonesia. Geomorphology, 273, 244-257.

Gong, L. 2013. Data-driven scale extrapolation: Estimating yearly discharge for a large region by small sub-basins. Hydrology and Earth System Sciences. 18. 10.5194/hess-18-343-2014.

683 Gran, K.B., 2012. Strong seasonality in sand loading and resulting feedbacks on sediment transport,
684 bed texture, and channel planform at Mount Pinatubo, Philippines. Earth Surf. Process. Landf. 37,
685 1012–1022. http://dx.doi.org/10.1002/esp.3241.
686 Gran, K.B., Montgomery, D.R., 2005. Spatial and temporal patterns in fluvial recovery following
687 volcanic eruptions: channel response to basin-wide sediment loading at Mount Pinatubo, Philippines.
688 Geol. Soc. Am. Bull. 117 (1–2), 195–211. http://dx.doi.org/10.1130/B25528.1
689 Gutierrez, A.G., Armesto, J.J., Aravena, J.C., Carmona, M., Carrasco, N.V., Christie, D.A., Peña,
690 M.P., Pérez, C., Huth, A., 2009. Structural and environmental characterization of old-growth
691 temperate rainforests of northern Chiloe Island, Chile: Regional and global relevance. Forest Ecol.
692 Manag., 258, 376-388.
693 Hickin, E.J. 1984. Vegetation and river channel dynamics. Canadian Geographer, XXVIII (2): 111-
694 126.
695 Hong, L.B., Davies, T.R.H., 1979. A study of stream braiding. Geol. Soc. Am. Bull. 90 (Part II),
696 1839–1859.
697 Howard, A.D., Keetch, M.E., Vincent, C.L., 1970. Topological and geometrical properties of braided
698 streams. Water Resour. Res., 6, 1674–1688.
699 Huang, C., Davis, L.S., Townshend, J.R.G. 2002. An Assessment of Support Vector Machines for
700 Land Cover Classification. International Journal of Remote Sensing 23(4): 725–49.
701 Hupp, C.R. 1992. Riparian vegetation recovery patterns following stream channelization: a
702 geomorphic perspective. Ecology, 73 (4): 1209-1226.
703 Inostroza, R., 2014. Impactos de la erupción del Volcán Chaiten en cauces asociados a tres cuencas
704 ubicadas en sus laderas norponientes. Thesis, Civil Engineering, Universidad Austral de Chile.
705 Valdivia, Chile, 62 p.
706 Julien, Y., Sobrino, J.A., Mattar, C., Ruescas, A.B., Jiménez-Muñoz, J.C., Sória, G., Hidalgo, V.,
707 Atitar, M., Franch, B., Cuenca, J., 2011. Temporal analysis of normalized difference vegetation index
708 (NDVI) and land surface temperature (LST) parameters to detect changes in the Iberian land cover
709 between 1981 and 2001. International Journal of Remote Sensing, 32 (7), 2057–2068.
710 Kavzoglu, T., Colkesen, I. 2009. A Kernel Functions Analysis for Support Vector Machines for Land
711 Cover Classification. International Journal of Applied Earth Observation and Geoinformation 11(5):
712 352–59.
713 Korup, O., Seidemann, J., Mohr, C. 2019. Increased landslide activity on forested hillslopes following
714 two recent volcanic eruptions in Chile. Nature Geoscience, https://doi.org/10.1038/s41561-019-0315-
715 9
716 Laben, C.A., Brower, B.V. 2000. Process for enhancing the spatial resolution of multispectral

imagery using pan-sharpening. United States Patent 6,011,875. Jan 4, 2000.
Lara, L., 2009. The 2008 eruption of the Chaitén Volcano, Chile: a preliminary report. Andean Geology, 36 (1), 125–129.
Major, J. J. and Lara, L.E., 2013. Overview of Chaitén Volcano, Chile, and its 2008–2009 eruption. Andean Geology, 40 (2), 196–215.
Major, J.J., Mark, L.E., 2006. Peak flow responses to landscape disturbances caused by the cataclysmic 1980 eruption of Mount St. Helens, Washington. Geol. Soc. Am. Bull. 118 (7-8), 938–958. http://dx.doi.org/10.1130/B25914.1
Major, J.J., Pierson, T.C., Hoblitt, R.P., Moreno, H., 2013. Pyroclastic density currents associated with the 2008–09 eruption of Chaitén Volcano (Chile): forest disturbances, deposits, and dynamics. Andean Geology, 40 (2), 324–358.
Major, J. J., Bertin, D., Pierson, T.C., Amigo, A., Iroumé, A., Ulloa, H., Castro, J., 2016. Extraordinary sediment delivery and rapid geomorphic response following the 2008–2009 eruption of Chaitén Volcano, Chile. Water Resources Research, 52.
Morresi, D., Vitali, A., Urbinati, C., Garbarino, M., 2019. Forest Spectral Recovery and Regeneration Dynamics in Stand-Replacing Wildfires of Central Apennines Derived from Landsat Time Series. Remote Sensing, 11, 308.
Pierson, T.C., Pringle, P.T., Cameron, K.A., 2011. Magnitude and timing of downstream channel aggradation and degradation in response to a dome-building eruption at Mount Hood, Oregon. Geol. Soc. Am. Bull. 123 (1–2), 3–20. http://dx.doi.org/10.1130/B30127.1.
Pierson, T., Major, J., Amigo, A., Moreno, H., 2013. Acute sedimentation response to rainfall following the explosive phase of the 2008–09 eruption of Chaitén volcano, Chile. Bull. Volcanol., 75 (5), 1–17.
Pierson, T. C., Major, J. J., 2014. Hydrogeomorphic effects of explosive volcanic eruptions on drainage basins, Ann. Rev. Earth Planet. Sci., 42, 469–507.
Pollmann, W., & Veblen, T. T. (2004). Nothofagus regeneration dynamics in south-central Chile: a test of a general model. Ecological Monographs, 74(4): 615-634.
Scheffler, D., Hollstein, A., Diedrich, H., Segl, K., Hostert, P. 2017. AROSICS: An Automated and Robust Open-Source Image Co-Registration Software for Multi-Sensor Satellite Data. Remote Sens. 9, 676.
Swanson, F.J., Jones, J.A., Crisafulli, C.M., Lara, A., 2013. Effects of volcanic and hydrologic processes on forest vegetation: Chaitén Volcano, Chile. Andean Geology, 40 (2), 359–391.
Teltscher, K., Fassnacht, F.E., 2018. Using multispectral landsat and sentinel-2 satellite data to investigate vegetation change at Mount St. Helens since the great volcanic eruption in 1980. Journal

751 of Mountain Science, 15(9), 1851-1867.
752 Tonon, A., Iroumé, A., Picco, L., Oss-Cazzador, D., Lenzi, M.A., 2017. Temporal variations of large
753 wood abundance and mobility in the Blanco River affected by the Chaitén volcanic eruption, southern
754 Chile. Catena, 156, 149-160.
755 Ulloa, H., Iroumé, A., Mao, L., Andreoli, A., Diez, S., Lara, L.E., 2015a. Use of remote imagery to
756 analyse changes in morphology and longitudinal large wood distribution in the Blanco River after the
757 2008 Chaitén volcanic eruption, southern Chile, Geogr. Ann., Ser. A, 97, 523–541.
758 Ulloa, H., Iroumé, A., Picco, L., Korup, O., Lenzi, M.A., Mao, L., Ravazzolo, D., 2015b. Massive
759 biomass flushing despite modest channel response in the Rayas River following the 2008 eruption of
760 Chaitén volcano, Chile. Geomorphology, 250, 397-406.
761 Ulloa, H., Iroumé, A., Picco, L., Mohr, C. H., Mazzorana, B., Lenzi, M. A., Mao, L., 2016. Spatial
762 analysis of the impacts of the Chaitén volcano eruption (Chile) in three fluvial systems. Journal of
763 South American Earth Sciences, 69, 213-225.
764 Umazano, A.M., Melchor, R.N., Bedatou, E., Krause, J.M., 2014. Fluvial response to sudden input
765 of pyroclastic sediments during the 2008-2009 eruption of the Chaitén Volcano (Chile): the role of
766 logjams. J. South Am. Earth Sci., 54, 140-157.
767 van Leeuwen, W.J. D., Casady, G.M., Neary, D.G., Bautista, S., Alloza, J.A., Carmel, Y., Wittenberg,
768 L., Malkinson, D., Orr, B.J., 2010. Monitoring post-wildfire vegetation response with remotely
769 sensed time-series data in Spain, USA and Israel. International Journal of Wildland Fire, 19, 75–93
770 Veblen, T. T., Alaback, P. B. 1996. A comparative review of forest dynamics and disturbance in the
771 temperate rainforests of North and South America. In *High-Latitude Rainforests and Associated*
772 *Ecosystems of the West Coast of the Americas* (pp. 173-213). Springer, New York, NY.
773 Veblen, T. T., Donoso, C., Kitzberger, T., & Rebertus, A. J. (1996). Ecology of southern Chilean and
774 Argentinean Nothofagus forests. The ecology and biogeography of Nothofagus forests, 10: 93-353.
775 Vericat, D., Brasington, J., Wheaton, J., Cowie, M., 2009. Accuracy assessment of aerial photographs
776 acquired using lighter-than-air blimps: low-cost tools for mapping river corridors. River Res. Appl.,
777 25, 985–1000.
778 Wilson, T.M., Cole, J.W., Stewart, C., Cronin, S.J., Johnston, D.M., 2011. Ash storms: impacts of
779 windremobilized volcanic ash on rural communities and agriculture following the 1991 Hudson
780 eruption, southern Patagonia, Chile. Bull. Volcan., 73, 223-239.
781